Advanced Photonics Research

ADVANCED PHOTONICS RESEARCH Open Access

www.adpr-journal.com

RESEARCH ARTICLE OPEN ACCESS

Omnidirectional and Directional Thermal Emission From Distinct Gradient-Doped InAs Multilayer Designs

Ke Ma[1] | Gokul Nanda Gopakumar[2] | Zhixiang Huang[1] | Sai Rahul Sitaram[1] | Stephanie Law[2,3,4,5] | Xi Wang[1]

[1]Department of Materials Science and Engineering, University of Delaware, Newark, Delaware, USA | [2]Department of Materials Science and Engineering, The Pennsylvania State University, University Park, Pennsylvania, USA | [3]Materials Research Institute, The Pennsylvania State University, University Park, Pennsylvania, USA | [4]Department of Physics, The Pennsylvania State University, University Park, Pennsylvania, USA | [5]Institute of Energy and the Environment, The Pennsylvania State University, University Park, Pennsylvania, USA

Correspondence: Stephanie Law (sal6149@psu.edu) | Xi Wang (wangxi@udel.edu)

Received: 22 July 2026 | **Revised:** 18 September 2026 | **Accepted:** 29 September 2026

Keywords: directional emission | gradient-doped films | omnidirectional emission | thermal emission control

Controlling thermal emission with tailored spectral and angular characteristics is essential for applications including thermophotovoltaics, radiative cooling, infrared sensing, and thermal camouflage. Existing demonstrations typically achieve either omnidirectional absorption or directional emission, often relying on patterned nanostructures that limit scalability. Here, we demonstrate two distinct classes of lithography-free, wafer-scale gradient-doped indium arsenide multilayers within a common material platform. Polarization-matched gradient-Epsilon-Near-Zero (ENZ) designs produce polarization-independent omnidirectional thermal emission near 9 and 11 μm, whereas angle-matched gradient-ENZ designs produce broadband transverse magnetic-polarized directional emission over the 7–10 and 10–15 μm ranges. These results demonstrate a scalable semiconductor multilayer framework in which carrier-density and layer-thickness engineering provide distinct routes to spectral, angular, and polarization-dependent thermal-emission control.

1 | Introduction

Tailored thermal emission underpins a wide range of technologies, including thermophotovoltaics (TPV) [1, 2], infrared sensing [3], thermal camouflage [4, 5], radiative cooling [6, 7], and smart windows [8, 9]. In TPV, spectral control aligns emitted wavelengths with the photovoltaic bandgap to maximize power conversion efficiency [10, 11]. In radiative cooling, both spectral and angular control help dissipate heat efficiently by directing thermal radiation within the atmospheric transparency windows [12, 13]. Likewise, angular control enhances performance in thermal camouflage and infrared detection by directing radiation into specific viewing angles, thereby reducing detectability and sharpening detection accuracy [14, 15].

Considerable progress has been made toward omnidirectional emission using Fabry-Pérot absorbers, metal-dielectric-metal stacks, and impedance-matched lossy films [16–18]. These structures achieve high, polarization-robust wide-angle emission by matching the effective surface impedance to free space [19, 20]. However, they are typically spectrally inflexible and exhibit angle-wavelength dispersion because the resonance wavelength shifts with incident angle [21, 22]. Other material platforms, including carbon-based emitters [23] and plasmonic nanostructures [24], offer strong emissivity intensity but still face challenges in achieving wide-angle robustness. Metamaterials such as electric split-ring resonator absorbers have shown significant promise as polarization-independent perfect absorbers for both transverse electric (TE) and transverse magnetic (TM) polarizations with an angular range of up to 60° [25, 26]. These approaches generally provide either strong emissivity or polarization-insensitive response over selected spectral or angular ranges. However, they typically remain limited by angle-dependent resonance shifts, narrow spectral tunability, reduced performance at oblique

This is an open access article under the terms of the Creative Commons Attribution License, which permits use, distribution and reproduction in any medium, provided the original work is properly cited.

© 2026 The Author(s). *Advanced Photonics Research* published by Wiley-VCH GmbH.

incidence, or complicated fabrication requirements that preclude large-area implementation [27–29].

Directional thermal emission presents an additional challenge because it requires precise engineering of both spectral and angular distributions. Traditional strategies that leverage surface plasmon polaritons (SPPs) [30], phonon-polaritonic structures [31], and/or photonic crystals [32] have shown substantial progress in spectral selectivity but typically function over narrow bandwidths with moderate emissivity. Epsilon-near-zero (ENZ) materials offer a promising alternative as they support a leaky TM-polarized mode, often referred to as the Berreman mode, that couples to free space at a characteristic angle when their permittivity is close to zero [33, 34]. In the long-wave infrared and near-infrared regions, conventional polaritonic oxides (e.g., SiO_2, Al_2O_3, and SiC) achieve this ENZ condition through their phonon-polariton resonances, but these materials are limited to narrow spectral regions that are determined by the fixed lattice-vibrational modes in polaritonic oxides [35]. Gradient-ENZ strategies broaden the concept by varying the ENZ wavelength through the film thickness by changing the film composition, allowing different wavelengths to experience ENZ at different depths at nearly the same angle [36, 37]. However, existing gradient-ENZ emitters remain constrained by limited tunability, spectral range, bandwidth, and material choices [36, 38, 39].

While gradient-ENZ strategies and semiconductor-based platforms have enabled omnidirectional absorption or directional thermal emission, these responses represent distinct design objectives with different spectral, angular, and polarization requirements. This motivates the development of a common material and growth platform in which different multilayer configurations can be engineered for these distinct emission behaviors.

Here, we demonstrate two distinct classes of lithography-free, wafer-scale gradient-doped InAs multilayers within a common material and growth platform. Polarization-matched gradient-ENZ designs are engineered to align the TE- and TM-polarized absorption bands at selected wavelengths, yielding polarization-independent omnidirectional thermal emission. In contrast, angle-matched gradient-ENZ designs distribute different ENZ wavelengths through the multilayer while maintaining broadband TM-polarized Berreman-mode emission near a common highly oblique angle, yielding directional emission over two designable wavelength ranges. These two design classes demonstrate how carrier-density and layer-thickness engineering within the same semiconductor material system can realize distinct spectral, angular, and polarization-dependent thermal-emission responses without lithographic patterning.

2 | Materials Platform

In this work, indium arsenide (InAs) is used as the base material. Doping InAs with silicon (Si) during molecular beam epitaxy (MBE) results in a tunable plasma wavelength across the mid-IR range, enabling effective control over the material's permittivity and optical response [40, 41]. Furthermore, InAs has one of the lowest optical losses and highest quality factors in the 5–10 μm range [42]. These properties allow InAs to support plasmonic or ENZ modes with low optical loss, making it highly advantageous for applications in broadband thermal emission control, angle-selective absorbers, and reconfigurable optical structures [41, 43]. Figure 1a,b schematically illustrate the polarization-matched and angle-matched gradient-ENZ design concepts investigated in this work, respectively.

The optical response of doped semiconductors is well described by the Drude model,

$$\varepsilon(\omega) = \varepsilon_s\left(1 - \frac{\omega_p^2}{\omega^2 + i\omega\Gamma}\right), \omega_p^2 = \frac{n_d e^2}{\varepsilon_s \varepsilon_0 m^*}$$

which expresses the complex permittivity in terms of the carrier scattering rate Γand plasma frequency ω_p. The plasma frequency depends on the electron effective mass m^* and the doping concentration n_d. Here, ε_0 is the vacuum permittivity and ε_s is the relative permittivity of the bulk, undoped semiconductor (12.3).

The real part of Si:InAs permittivity as a function of doping concentration and wavelength is shown in Figure 1c. The red curve in Figure 1c indicates the ENZ wavelength. For doping concentrations from 0.5 to $5\times10^{25}\,m^{-3}$, ENZ gradient behavior is achieved in the MIR range. The corresponding imaginary part

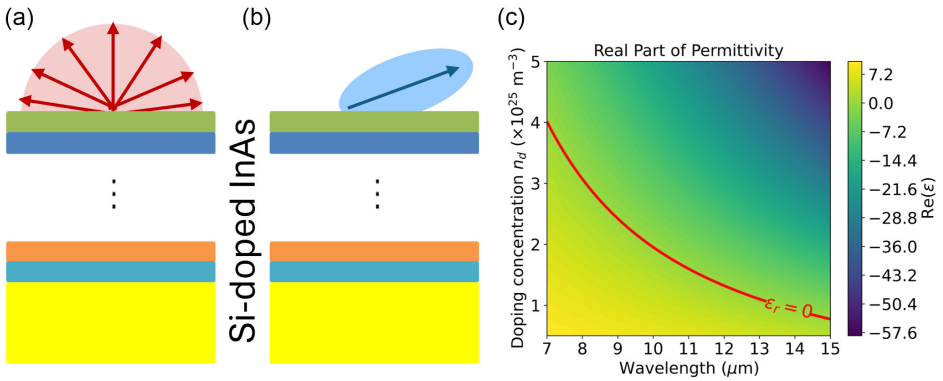

FIGURE 1 | Schematic illustrations of the two distinct gradient-doped InAs multilayer design classes investigated in this work: (a) polarization-matched gradient-ENZ design for polarization-independent omnidirectional emission and (b) angle-matched gradient-ENZ design for broadband TM-polarized directional emission. (c) Real part of the Si:InAs permittivity as a function of wavelength and doping concentration. The red curve marks the ENZ condition, where $\mathrm{Re}(\varepsilon)=0$.

26999293, 2026, 10, Downloaded from https://advanced.onlinelibrary.wiley.com/doi/10.1002/adpr.70292 by University Of Delaware Library, Wiley Online Library on [23/10/2026]. See the Terms and Conditions (https://onlinelibrary.wiley.com/terms-and-conditions) on Wiley Online Library for rules of use; OA articles are governed by the applicable Creative Commons License

of the permittivity, presented using a logarithmic color scale, is provided in the Supporting Information. Across the range of interest, the imaginary part of the permittivity is relatively low. These data serve as the foundation for structural design in the rest of the paper, where each layer's doping is tailored to place its ENZ resonance at a desired spectral position.

The thermal-emission response of the multilayer platform is evaluated through its calculated and measured optical response. Reflectance R is used to indirectly determine the directional emissivity. Further details of the reflectance definition, Fourier transform infrared spectroscopy (FTIR) measurements, and emissivity calculation are provided in Section 6 and Supporting Information.

3 | Design

In principle, a medium whose permittivity remains near zero can act as a directional emitter for TM-polarized light. In practice, ENZ behavior in real materials occurs only near specific electronic or phonon resonances, meaning that the $\varepsilon \approx 0$ condition appears over a narrow spectral band rather than across a wide wavelength range. To overcome this limitation, we propose the gradient-ENZ platform, in which the material's permittivity is spatially graded by tailoring the carrier-density profile. By distributing the ENZ condition along the film thickness, different wavelengths encounter $\varepsilon \approx 0$ at different depths while maintaining phase matching to approximately the same external angles, enabling broadband, angle-selective thermal emission. The initial thickness of each ENZ layer is based on the Berreman thickness equation

$$\text{thickness} = \frac{\lambda}{2\pi}\frac{\cos\theta}{\sin^2\theta}\left(Im\left\{\frac{-1}{\varepsilon(\lambda)}\right\}\right)^{-1}_{\max}$$

Here, λ is the ENZ wavelength, θ is the emission angle, and is is the complex permittivity of ENZ film [35]. This expression provides an initial thickness estimate for an individual ENZ layer. The final multilayer design requires three additional adjustments to achieve the targeted spectral, angular, and polarization-dependent response.

First, a lightly doped InAs spacer layer with a carrier concentration of $1\times10^{23}\,m^{-3}$ is inserted between the active Si:InAs stacks as a dielectric gap layer. Without this spacer, a sufficiently thick and continuous gradient-ENZ stack can support an unwanted broadband TM-polarized leaky response, which reduces angular selectivity and may drive the structure toward a more omnidirectional response [35, 44]. The spacer separates the active ENZ sections and modifies their electromagnetic coupling and multilayer interference, thereby suppressing this unwanted response while preserving the desired interaction among the ENZ layers.

Second, the individual layer thicknesses are refined beyond the initial values obtained from Berreman thickness expression. The Berreman relation describes an approximate single-layer TM-polarized coupling condition and does not fully capture interactions among multiple ENZ layers or the TE-polarized response. The thicknesses were therefore adjusted using the calculated response of the complete stack to achieve the intended angular and spectral characteristics. For the polarization-matched designs, this refinement is used to align the TE- and TM-polarized absorption bands at the target wavelength. For the angle-matched designs, the layer thicknesses are selected to maintain broadband TM-polarized emission near the target angle while suppressing the corresponding TE-polarized response.

Third, a 1000-nm thick highly doped InAs virtual substrate with a doping concentration of $1\times10^{26}\,m^{-3}$ is incorporated beneath the active multilayer stack as an optically opaque back reflector. This layer suppresses transmission and enhances absorption within the active structure. A thickness of 1000 nm is sufficient to suppress transmission for wavelengths longer than 5.48 μm, covering the full spectral range considered in this work [41].

To calculate the optical response of the layered Si-doped InAs structures, we employ the transfer matrix method (TMM), which models plane-wave propagation through stratified media. The wavelength- and angle-dependent reflectance R, transmittance T, and absorptance $A = 1 - R - T$ are then obtained. For the optically opaque structures considered here, $T \approx 0$, and therefore, the directional emissivity under thermal equilibrium is $\varepsilon = A \approx 1 - R$ [45, 46].

Leveraging these principles, we implement two distinct gradient-ENZ design classes within the same Si-doped InAs material system. For the polarization-matched designs (Structures 1 and 2), the individual layer thicknesses are refined using the calculated multilayer response to align the TE- and TM-polarized absorption bands at the target wavelengths of approximately 9 and 11 μm, respectively. For the angle-matched designs (Structures 3 and 4), layers spanning different ENZ wavelengths are configured so that their TM-polarized Berreman responses remain concentrated near the target highly oblique angle over the 7–10 and 10–15 μm ranges, respectively. The doping and thickness profiles of Structures 1–4 are detailed in Tables S2–S4. The corresponding doping concentration profiles as a function of thickness are summarized in Figure 2. Figure 2a compares the polarization-matched designs, Structures 1 and 2, whereas Figure 2b compares the angle-matched designs, Structures 3 and 4.

In practice, small deviations in doping concentration are inevitable during materials synthesis, including MBE growth, where slight fluctuations in dopant flux can lead to unintended shifts in carrier concentration. Since the plasma wavelength and the scattering rate are highly sensitive to doping, this results in deviations in optical characteristics. To evaluate the fabrication tolerance of the proposed design, we perform a robustness analysis on Structure 1, accounting for variations in carrier concentration during growth. Details are provided in the Supporting Information. Overall, the results show that even under relatively large doping fluctuations (±20%), the designed structure maintains its angular- and polarization-robust absorption behavior, with the omnidirectional emission band remaining well preserved. This confirms that the gradient ENZ platform is tolerant to fabrication-induced variations and is therefore well suited for practical implementation in omnidirectional thermal management systems.

26999293, 2026, 10, Downloaded from https://advanced.onlinelibrary.wiley.com/doi/10.1002/adpr.70292 by University Of Delaware Library, Wiley Online Library on [23/10/2026]. See the Terms and Conditions (https://onlinelibrary.wiley.com/terms-and-conditions) on Wiley Online Library for rules of use; OA articles are governed by the applicable Creative Commons License

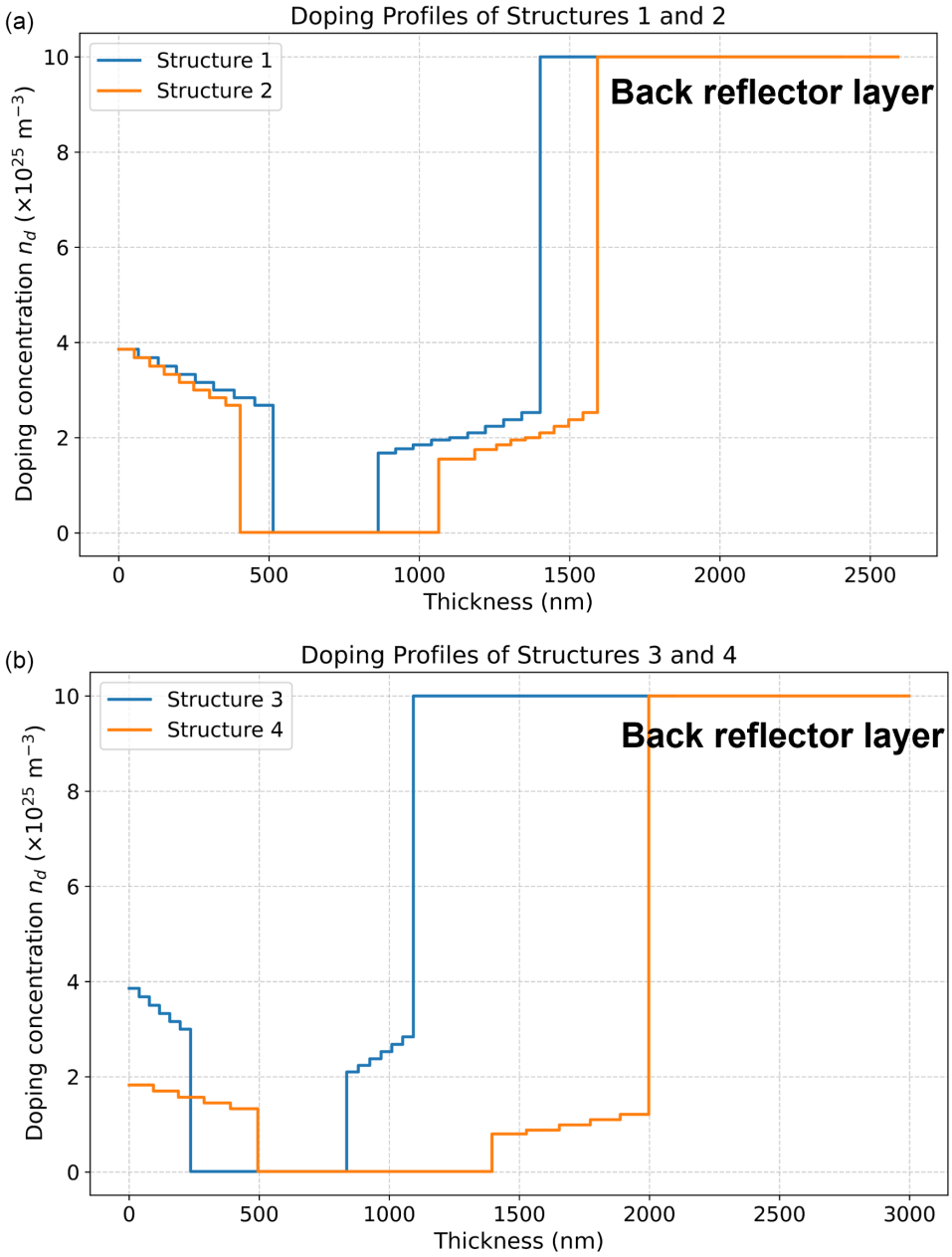

FIGURE 2 | Doping concentration profiles as a function of cumulative thickness for the four gradient-doped InAs multilayer structures. (a) Polarization-matched gradient-ENZ designs targeting polarization-independent omnidirectional emission near 9 μm (Structure 1, blue) and 11 μm (Structure 2, orange). (b) Angle-matched gradient-ENZ designs targeting broadband TM-polarized directional emission over 7–10 μm (Structure 3, blue) and 10–15 μm (Structure 4, orange). The profiles extend from the top surface toward the substrate, and the highly doped InAs back-reflector layer is indicated.

4 | Results

We quantified absorptance indirectly from reflectance rather than measuring thermal emission or transmission directly because reflectance measurements are faster, have higher SNR, and are more reproducible in a standard FTIR reflection geometry. For the present stacks, the thickness of the $1\times10^{26}\,\mathrm{m}^{-3}$ highly doped virtual substrate is ~1000 nm. In practice, such a thickness is enough to reflect all light with a wavelength longer than 5.48 μm [41], making transmission negligible, so by energy conservation

$$A(\lambda,\,\theta)\;=\;1-R(\lambda,\,\theta)-T(\lambda,\,\theta)\;\approx\;1-\;R(\lambda,\,\theta)$$

Under these conditions, Kirchhoff's law gives directional emissivity equal to A, allowing emissivity to be inferred from the reflectance without additional heating or emission hardware [47]. Accordingly, both the simulated and experimentally derived emissivity spectra and maps presented in this article were obtained using

$$\varepsilon(\lambda,\,\theta)\approx 1-\;R(\lambda,\,\theta)$$

The experimental results therefore represent reflectance-derived emissivity rather than direct heated-stage thermal-emission measurements.

26999293, 2026, 10, Downloaded from https://advanced.onlinelibrary.wiley.com/doi/10.1002/adpr.70292 by University Of Delaware Library, Wiley Online Library on [23/10/2026]. See the Terms and Conditions (https://onlinelibrary.wiley.com/terms-and-conditions) on Wiley Online Library for rules of use; OA articles are governed by the applicable Creative Commons License

Structures 1 and 2 represent the polarization-matched gradient-ENZ design class and target polarization-independent omnidirectional thermal emission near 9 and 11 μm, respectively. Structure 1 consists of a 19-layer Si-doped InAs stack with a graded doping profile, while Structure 2 uses the same graded doping profile with modified layer thicknesses to shift the target emission wavelength. To compare the spectral and angular responses of the two structures directly, Figure 3 presents the simulated and experimentally derived emissivity maps organized by polarization. Figure 3a–d show the TE-polarized responses of Structures 1 and 2, Figure 3e–h show the corresponding TM-polarized responses, and Figure 3i,j compare their angle-dependent emissivities near the respective emission wavelengths.

Under TE polarization, both structures exhibit well-defined, nearly angle-invariant high-emissivity bands across the measured angular range. For Structure 1, the simulated response is centered near 9 μm, while the experimental band exhibits a blueshift of approximately 0.5 μm (Figure 3a,b). For Structure 2, the corresponding response shifts to approximately 11 μm, with the experimental spectrum showing a smaller redshift of approximately 0.2 μm relative to the simulation (Figure 3c,d). These spectral shifts are consistent with the expected <20 % doping deviation or 9 % plasma wavelength variation identified in the tolerance analysis. This shift may be due to growth-related variations such as shifts in growth rate or dopant flux during deposition. It could also be due to the small conduction band offset between InAs layers with different doping densities, which can lead to electrons "leaking" across layer boundaries [48]. The comparison also illustrates that modifying the multilayer thicknesses shifts the omnidirectional emission band while preserving its broad angular response.

Under TM polarization, both structures retain broad high-emissivity responses over the measured angular range (Figure 3e–h), although the experimental features are broader and less uniform than their simulated counterparts. For Structure 1, the experimental TM response preserves the overall spectral and angular trend of the simulated band near 9 μm but exhibits increased broadening. Structure 2 shows a similar behavior near 11 μm, together with mild interference features and reduced spectral contrast. The greater experimental broadening under TM polarization is consistent with the stronger sensitivity of the TM response to variations in doping profile, layer thickness, and refractive index. Additional measurement effects such as beam divergence, imperfect polarization separation, and detector angle averaging can further contribute to the observed spectral broadening and noise.

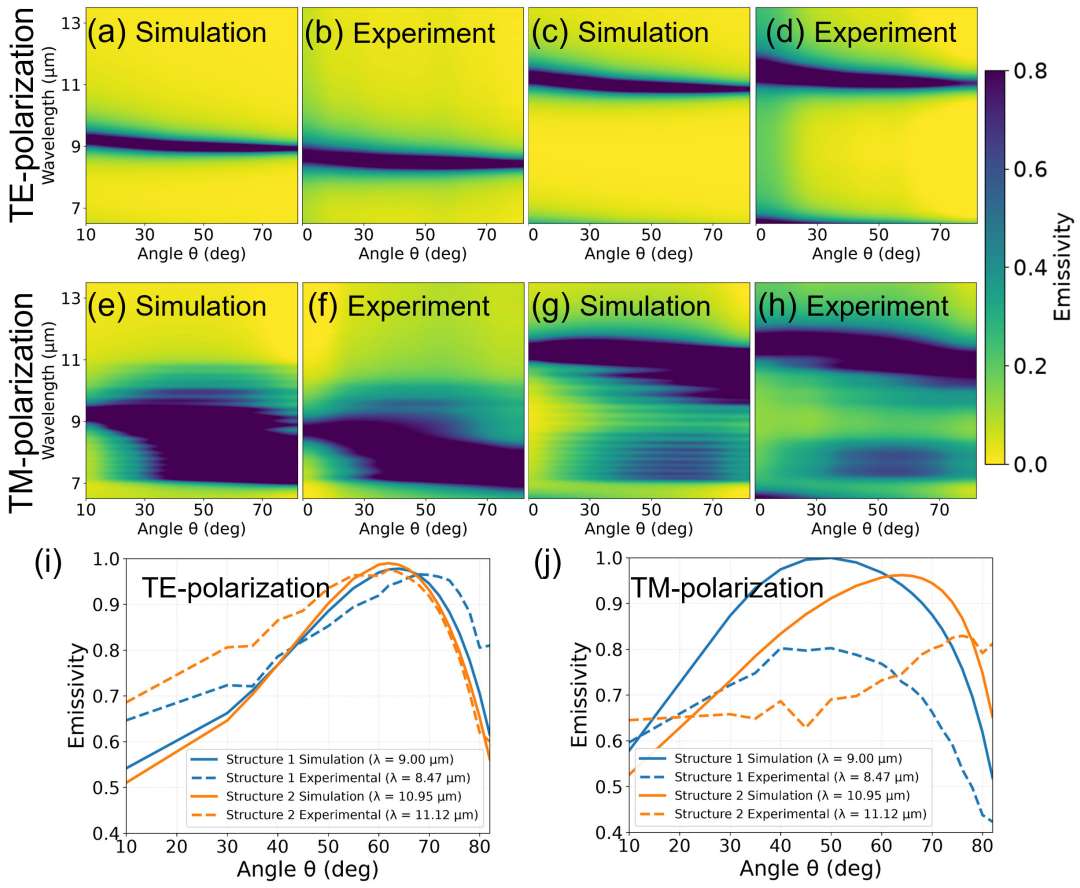

FIGURE 3 | Polarization-independent omnidirectional thermal emission of the polarization-matched gradient-ENZ designs targeting approximately 9 μm (Structure 1) and 11 μm (Structure 2). (a–d) TE-polarized emissivity maps: (a) simulated and (b) experimental results for Structure 1, and (c) simulated and (d) experimental results for Structure 2. (e–h) TM-polarized emissivity maps: (e) simulated and (f) experimental results for Structure 1, and (g) simulated and (h) experimental results for Structure 2. (i,j) Angle-dependent emissivity near the corresponding emission wavelengths for Structures 1 and 2 under (i) TE and (j) TM polarization, comparing experimental and simulated results.

26999293, 2026, 10, Downloaded from https://advanced.onlinelibrary.wiley.com/doi/10.1002/adpr.70292 by University Of Delaware Library, Wiley Online Library on [23/10/2026]. See the Terms and Conditions (https://onlinelibrary.wiley.com/terms-and-conditions) on Wiley Online Library for rules of use; OA articles are governed by the applicable Creative Commons License

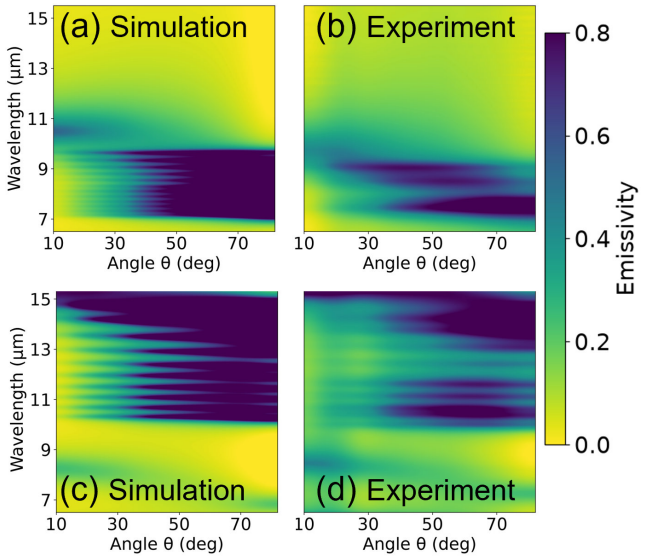

FIGURE 4 | Broadband TM-polarized directional thermal emission of the angle-matched gradient-ENZ designs. (a,b) Structure 3, designed for the 7–10 μm wavelength range: (a) simulated and (b) experimental emissivity maps. (c,d) Structure 4, designed for the 10–15 μm wavelength range: (c) simulated and (d) experimental emissivity maps. Emissivity is plotted as a function of wavelength and incidence angle, showing the directional high-emissivity response at highly oblique angles.

The angle-dependent emissivity curves in Figure 3i,j provide a direct comparison of Structures 1 and 2 under TE and TM polarization, respectively. Both structures maintain strong emissivity over a broad angular range from 10° to 80° near their corresponding emission bands, demonstrating that the spectral shift from approximately 9–11 μm is achieved without eliminating the wide-angle response. Taken together, the spectral maps and angular line cuts demonstrate the tunability of the polarization-matched design through multilayer parameter engineering while retaining polarization-independent, wide-angle thermal emission.

The angle-matched gradient-ENZ design class is represented by Structures 3 and 4, which use engineered doping and thickness profiles to support broadband TM-polarized directional emission at highly oblique angles. Structure 3 contains 14 layers optimized for the 7–10 μm range, while Structure 4 uses 12 layers to target 10–15 μm.

To evaluate the predicted directional thermal emission performance, experimental emissivity inferred from the angle-resolved FTIR reflectance measurements was compared against simulated spectra under TM (*p*-polarized) illumination. The simulated and experimental TM-polarized emissivity maps for both angle-matched designs are compared in Figure 4. Figure 4a,b showshe simulated and experimental responses of Structure 3, respectively, while Figure 4c,d showshe corresponding responses of Structure 4.

For Structure 3 shown in Figure 4a,b, a systematic blue shift of approximately 0.45 μm is observed in the experimental spectra compared with the simulation. This behavior mirrors that of Structure 1 and can be attributed to a less than 20 % variation in carrier concentration, corresponding to a 9 % decrease in plasma wavelength. Since Structures 1 and 3 were fabricated within the same MBE growth batch, the similar magnitude and direction of the shift may indicate a reproducible calibration offset intrinsic to that run. In the simulation shown in Figure 4a, a pronounced low-reflectance band appears between 7–10 μm, centered around 75°, indicating strong directional thermal emission, with the simulated emissivity exceeding 0.8. The experimental map shown in Figure 4b retains this feature, though with a slightly diminished and broadened emissivity peak, corresponding to a measured emissivity above 0.6. Despite minor fabrication deviations, the directional emission behavior remains clearly preserved.

For Structure 4 shown in Figure 4c,d, the emissivity spectra display a systematic red shift of approximately 0.3 μm relative to the simulation, consistent with the trend observed in Structure 2. This shift is likely due to a minor underestimation of the doping concentration, well below 20%. Since Structures 2 and 4 were also grown in the same MBE batch, the similar redshift magnitude further supports the batch-to-batch consistency and predictability of the calibration offsets. Both the simulated results shown in Figure 4c and experimental results shown in Figure 4d exhibit a tailored high-emissivity band spanning 10–15 μm centered near 75°, confirming the realization of directional thermal emission in this longer wavelength range.

Overall, these 2D plots illustrate that the essential directional emission characteristics, including spectral range, angular selectivity, and peak emissivity, are successfully realized in practice, closely aligning with simulation expectations. This agreement further underscores the robustness of the multilayer ENZ design against real-world fabrication tolerances and supports the feasibility of deploying such structures in thermal photonic applications.

The residual mismatch between experimental and simulated spectra in all four structures mainly arises from three factors: (1) growth-related fluctuations, (2) measurement uncertainties, and (3) limitations of the fitting model. During MBE growth, even slight variations in dopant flux and fluctuations in dopant cell temperature can induce 20% deviations in carrier concentration, shifting the plasma frequency and scattering rate and causing noticeable spectral blue- or red-shifts. Experimentally, instrumental imperfections such as finite beam divergence, limited polarizer extinction ratio, and imperfect alignment can broaden or slightly offset spectral features. Furthermore, the Drude-based dielectric model used to derive the refractive index (permittivity) of Si-doped InAs may not fully capture the behavior of the specific films used as its parameters were fitted to literature data. To address these issues, future improvements should emphasize comprehensive control and characterization at every stage. For example, a more stabilized dopant cell temperature is expected to provide more accurate doping profiles. On the measurement side, improved calibration of the FTIR system, including incident angle alignment and precise polarization control, will further enhance the consistency between experimental and simulated results. By implementing these improvements, the mismatch between experiment and simulation is expected to be largely reduced, leading to near-perfect spectral alignment. Importantly, across all four structures, the observed experimental shifts remain within the ±20% tolerance analysis in the previous section. This confirms

26999293, 2026, 10, Downloaded from https://advanced.onlinelibrary.wiley.com/doi/10.1002/adpr.70292 by University Of Delaware Library, Wiley Online Library on [23/10/2026]. See the Terms and Conditions (https://onlinelibrary.wiley.com/terms-and-conditions) on Wiley Online Library for rules of use; OA articles are governed by the applicable Creative Commons License

that the deviations in plasma wavelength and doping concentration are fully explained by fabrication variability, underscoring both the robustness of the multilayer ENZ design and its practical feasibility for thermal photonic applications.

5 | Conclusion

We demonstrate two distinct gradient-ENZ multilayer design classes within a common Si-doped InAs material and growth platform, enabling polarization-independent omnidirectional emission and broadband TM-polarized directional emission in different structures. The results establish carrier-density and multilayer engineering as a scalable route to tailoring spectral, angular, and polarization-dependent thermal emission. Compared with patterned metasurfaces and phonon-limited oxide ENZ systems, the Si-doped InAs approach is lithography-free and compatible with wafer-scale epitaxial growth. Because the ENZ response is controlled through electronic carrier engineering rather than fixed lattice-vibrational resonances, the platform provides substantial flexibility in positioning and distributing ENZ wavelengths across the mid-infrared. Together, these results establish gradient-doped semiconductor multilayers as a versatile framework for complementary forms of thermal-emission control.

6 | Methods

6.1 | Sample Growth

Synthesis of the Si-doped InAs films was performed using a Veeco GenXplor molecular beam epitaxy system. Dual-zone Knudsen effusion cells were used for indium and bismuth, a single-zone effusion cell for silicon, and a valved cracker for arsenic. All samples were grown at 450 °C (measured using a pyrometer) on single-side-polished undoped InAs (100) substrates. InAs was grown at a fast growth rate of 1.2 μm/hr, which improves the incorporation of the Si dopants. In addition, all Si-doped layers had an additional Bi flux (beam equivalent pressure ratio of Bi:In of 3%). A small Bi flux acts as a surfactant, lowering the scattering rate and further improving Si incorporation [40, 49].

Calibration of the Si-doping density was done on 1.5 μm-thick Si-doped InAs films grown on undoped InAs substrates. A Bruker Vertex 70 V Fourier transform infrared spectrometer was used to collect reflection spectra of the calibration films at a 10° incident angle using a DTGS detector with a spectral resolution of 4 cm^{-1} and a scan velocity of 10 kHz. The data is normalized to the reflection from a gold mirror at 10°. The plasma frequency and scattering rate are extracted from the reflection data using a transfer matrix method in which the Si:InAs is treated using the Drude model [41]. The calibrated and literature-derived relationships among doping concentration, plasma frequency, and scattering rate are summarized in Table S1 [40, 50].

6.2 | FTIR Characterization

Postgrowth samples were measured using a Fourier-transform infrared spectrometer equipped with a variable-angle reflection stage to study angle-resolved specular reflectance under vacuum at room temperature (23°C). Reflection accessories were used to acquire reflection spectra at 10°, 30°–60° (every 5°), and 62°–82° (every 2°), respectively. A wire-grid polarizer is used to select TE- or TM-polarization. Both the gold reference and the sample reflections were acquired under identical incident angles, polarizer angles, temperature, and vacuum conditions to ensure consistency. Spectra were referenced to an evaporated Au mirror to remove the instrument response, yielding absolute reflectance $R(\lambda, \theta) = \frac{I_{\text{sample}}(\lambda, \theta)}{I_{\text{Au}}(\lambda, \theta)}$.

Acknowledgments

This research was supported in part by the U.S. National Science Foundation under award ECCS-2102027. This work was supported in part by the University of Delaware's AI Center for Excellence. The use of facilities and instrumentation supported by the U.S. National Science Foundation through the University of Delaware Materials Research Science and Engineering Center under award no. DMR-2011824.

Funding

This study was supported by the U.S. National Science Foundation Division of Electrical, Communications, and Cyber Systems (2102027), Division of Materials Research (2011824), and University of Delaware's AI Center for Excellence.

Conflicts of Interest

The authors declare no conflicts of interest.

Data Availability Statement

The data that support the findings of this study are available from the corresponding author upon reasonable request.

References

1. Q. Wang, T. Liu, L. Li, et al., "Ultra-Broadband Directional Thermal Emission," *Nanophotonics* 13 (2024): 793–801, https://doi.org/10.1515/nanoph-2023-0742.

2. E. Sakr and P. Bermel, "Thermophotovoltaics With Spectral and Angular Selective Doped-Oxide Thermal Emitters," *Optics Express* 25 (2017): A880–A895, https://doi.org/10.1364/OE.25.00A880.

3. K. D. Hakkel, M. Petruzzella, F. Ou, et al., "Integrated Near-Infrared Spectral Sensing," *Nature Communications* 13 (2022): 103, https://doi.org/10.1038/s41467-021-27662-1.

4. H. Zhu, Q. Li, C. Zheng, et al., "High-Temperature Infrared Camouflage With Efficient Thermal Management," *Light: Science & Applications* 9 (2020): 60, https://doi.org/10.1038/s41377-020-0300-5.

5. R. Hu, W. Xi, Y. Liu, et al., "Thermal Camouflaging Metamaterials," *Materials Today* 45 (2021): 120–141, https://doi.org/10.1016/j.mattod.2020.11.013.

6. J. Zhou, T. G. Chen, Y. Tsurimaki, et al., "Angle-Selective Thermal Emitter for Directional Radiative Cooling and Heating," *Joule* 7 (2023): 2830–2844, https://doi.org/10.1016/j.joule.2023.10.013.

7. A. P. Raman, M. A. Anoma, L. Zhu, E. Rephaeli, and S. Fan, "Passive Radiative Cooling Below Ambient Air Temperature Under Direct Sunlight," *Nature* 515 (2014): 540–544, https://doi.org/10.1038/nature13883.

8. H. Sentjens, A. J. J. Kragt, A. P. H. J. Schenning, and M. G. Debije, "Recent Advances in Solar Infrared Light Regulating Smart Windows Based on Organic Materials," *Responsive Materials* 1 (2023): e20230006, https://doi.org/10.1002/rpm.20230006.

26999293, 2026, 10, Downloaded from https://advanced.onlinelibrary.wiley.com/doi/10.1002/adpr.70292 by University Of Delaware Library, Wiley Online Library on [23/10/2026]. See the Terms and Conditions (https://onlinelibrary.wiley.com/terms-and-conditions) on Wiley Online Library for rules of use; OA articles are governed by the applicable Creative Commons License

9. W. Meng, J. Wang, and L. Jiang, "Recent Advances in Photochromic Smart Windows Based on Inorganic Materials," *Responsive Materials* 2 (2024): e20240001, https://doi.org/10.1002/rpm.20240001.

10. M. R. S. Dias, T. Gong, M. A. Duncan, et al., "Photonics Roadmap for Ultra-High-Temperature Thermophotovoltaics," *Joule* 7 (2023): 2209–2227, https://doi.org/10.1016/j.joule.2023.08.015.

11. S. Molesky, C. J. Dewalt, and Z. Jacob, "High Temperature Epsilon-Near-Zero and Epsilon-Near-Pole Metamaterial Emitters for Thermophotovoltaics," *Optics Express* 21 (2013): A96–A110, https://doi.org/10.1364/OE.21.000A96.

12. F. Xie, W. Jin, J. R. Nolen, et al., "Subambient Daytime Radiative Cooling of Vertical Surfaces," *Science* 386 (2024): 788–794, https://doi.org/10.1126/science.adn2524.

13. K. Tang, K. Dong, J. Li, et al., "Temperature-Adaptive Radiative Coating for All-Season Household Thermal Regulation," *Science* 374 (2021): 1504–1509, https://doi.org/10.1126/science.abf7136.

14. J. A. Mason, S. Smith, and D. Wasserman, "Strong Absorption and Selective Thermal Emission From a Midinfrared Metamaterial," *Applied Physics Letters* 98 (2011): 241105, https://doi.org/10.1063/1.3600779.

15. N. Liu, M. Mesch, T. Weiss, M. Hentschel, and H. Giessen, "Infrared Perfect Absorber and Its Application as Plasmonic Sensor," *Nano Letters* 10 (2010): 2342–2348, https://doi.org/10.1021/nl9041033.

16. M. A. Kats, R. Blanchard, S. Ramanathan, and F. Capasso, "Thin-Film Interference in Lossy, Ultra-Thin Layers," *Optics & Photonics News* 25 (2014): 40–47, https://doi.org/10.1364/OPN.25.1.000040.

17. H. Kocer, S. Butun, Z. Li, and K. Aydin, "Reduced Near-Infrared Absorption Using Ultra-Thin Lossy Metals in Fabry-Perot Cavities," *Scientific Reports* 5 (2015): 8157, https://doi.org/10.1038/srep08157.

18. H. Song, L. Guo, Z. Liu, et al., "Nanocavity Enhancement for Ultra-Thin Film Optical Absorber," *Advanced Materials* 26 (2014): 2737–2743, https://doi.org/10.1002/adma.201305793.

19. P. Wu, C. Zhang, Y. Tang, B. Liu, and L. Lv, "A Perfect Absorber Based on Similar Fabry-Perot Four-Band in the Visible Range," *Nanomaterials* 10 (2020): 488, https://doi.org/10.3390/nano10030488.

20. Y. Zhang, X. Sun, L. Liu, G. Qin, H. Yu, and Z. Li, "A Perfect Absorber Based on a VO_2-Tunable Fabry-Perot Cavity: An Analysis of Periodic Oscillation Absorption Characteristics," *Physica Scripta* 99 (2024): 095533, https://doi.org/10.1088/1402-4896/ad6d0c.

21. C.-H. Lin, R.-L. Chern, and H.-Y. Lin, "Polarization-Independent Broad-Band Nearly Perfect Absorbers in the Visible Regime," *Optics Express* 19 (2011): 415–424, https://doi.org/10.1364/OE.19.000415.

22. W. Zhou, K. Li, C. Song, et al., "Polarization-Independent and Omnidirectional Nearly Perfect Absorber With Ultra-Thin 2D Subwavelength Metal Grating in the Visible Region," *Optics Express* 23 (2015): A413–A418, https://doi.org/10.1364/OE.23.00A413.

23. O. Salihoglu, H. B. Uzlu, O. Yakar, et al., "Graphene-Based Adaptive Thermal Camouflage," *Nano Letters* 18 (2018): 4541–4548, https://doi.org/10.1021/acs.nanolett.8b01746.

24. C. Zhang and T. Ding, "Active Plasmonic Nanodevices: From Basic Principles to Emerging Applications," *Responsive Materials* 2 (2024): e20240024, https://doi.org/10.1002/rpm.20240024.

25. H. Tao, C. M. Bingham, D. Pilon, et al., "A Dual Band Terahertz Metamaterial Absorber," *Journal of Physics D: Applied Physics* 43 (2010): 225102, https://doi.org/10.1088/0022-3727/43/22/225102.

26. Y. Bai, L. Zhao, D. Ju, Y. Jiang, and L. Liu, "Wide-Angle, Polarization-Independent and Dual-Band Infrared Perfect Absorber Based on L-Shaped Metamaterial," *Optics Express* 23 (2015): 8670–8680, https://doi.org/10.1364/OE.23.008670.

27. T. V. Teperik, F. J. García de Abajo, A. G. Borisov, et al., "Omnidirectional Absorption in Nanostructured Metal Surfaces," *Nature Photonics* 2 (2008): 299–301, https://doi.org/10.1038/nphoton.2008.76.

28. Z. Li, E. Palacios, S. Butun, H. Kocer, and K. Aydin, "Omnidirectional, Broadband Light Absorption Using Large-Area, Ultrathin Lossy Metallic Film Coatings," *Scientific Reports* 5 (2015): 15137, https://doi.org/10.1038/srep15137.

29. K. Aydin, V. E. Ferry, R. M. Briggs, and H. A. Atwater, "Broadband Polarization-Independent Resonant Light Absorption Using Ultrathin Plasmonic Super Absorbers," *Nature Communications* 2 (2011): 517, https://doi.org/10.1038/ncomms1528.

30. T. Ribaudo, D. W. Peters, A. R. Ellis, P. S. Davids, and E. A. Shaner, "Highly Directional Thermal Emission From Two-Dimensional Silicon Structures," *Optics Express* 21 (2013): 6837–6844, https://doi.org/10.1364/OE.21.006837.

31. G. Lu, C. R. Gubbin, J. R. Nolen, et al., "Engineering the Spectral and Spatial Dispersion of Thermal Emission via Polariton-Phonon Strong Coupling," *Nano Letters* 21 (2021): 1831–1838, https://doi.org/10.1021/acs.nanolett.0c04767.

32. Y. Guo and S. Fan, "Narrowband Thermal Emission From a Uniform Tungsten Surface Critically Coupled With a Photonic Crystal Guided Resonance," *Optics Express* 24 (2016): 29896–29907, https://doi.org/10.1364/OE.24.029896.

33. S. Vassant, J.-P. Hugonin, F. Marquier, and J.-J. Greffet, "Berreman Mode and Epsilon Near Zero Mode," *Optics Express* 20 (2012): 23971–23977, https://doi.org/10.1364/OE.20.023971.

34. Z. Sakotic, A. Krasnok, N. Cselyuszka, N. Jankovic, and A. Alú, "Berreman Embedded Eigenstates for Narrow-Band Absorption and Thermal Emission," *Physical Review Applied* 13 (2020): 064073, https://doi.org/10.1103/PhysRevApplied.13.064073.

35. Y. Ying, B. Ma, J. Yu, et al., "Whole LWIR Directional Thermal Emission Based on ENZ Thin Films," *Laser & Photonics Reviews* 16 (2022): 2200018, https://doi.org/10.1002/lpor.202200018.

36. J. S. Hwang, J. Xu, and A. P. Raman, "Simultaneous Control of Spectral and Directional Emissivity With Gradient Epsilon-Near-Zero InAs Photonic Structures," *Advanced Materials* 35 (2023): 2302956, https://doi.org/10.1002/adma.202302956.

37. J. Xu, J. Mandal, and A. P. Raman, "Broadband Directional Control of Thermal Emission," *Science* 372 (2021): 393–397, https://doi.org/10.1126/science.abc5381.

38. S. McSherry and A. Lenert, "Design of a Gradient Epsilon-Near-Zero Refractory Metamaterial With Temperature-Insensitive Broadband Directional Emission," *Applied Physics Letters* 121 (2022): 191702, https://doi.org/10.1063/5.0122535.

39. J. S. Hwang, J. Xu, and A. P. Raman, "Thermally Tunable Angular Selectivity of Broadband Directional Thermal Emission," *Nano Letters* 25 (2025): 8064–8071, https://doi.org/10.1021/acs.nanolett.5c02197.

40. S. Law, D. C. Adams, A. M. Taylor, and D. Wasserman, "Mid-Infrared Designer Metals," *Optics Express* 20 (2012): 12155–12165, https://doi.org/10.1364/OE.20.012155.

41. S. Law, L. Yu, and D. Wasserman, "Epitaxial Growth of Engineered Metals for Mid-Infrared Plasmonics," *Journal of Vacuum Science & Technology B* 31 (2013): 03C121, https://doi.org/10.1116/1.4797487.

42. Y. Zhong, S. D. Malagari, T. Hamilton, and D. Wasserman, "Review of Mid-Infrared Plasmonic Materials," *Journal of Nanophotonics* 9 (2015): 093791, https://doi.org/10.1117/1.jnp.9.093791.

43. J. B. Khurgin and A. Boltasseva, "Reflecting Upon the Losses in Plasmonics and Metamaterials," *MRS Bulletin* 37 (2012): 768–779, https://doi.org/10.1557/mrs.2012.173.

44. L. Nordin, O. Dominguez, C. M. Roberts, et al., "Mid-Infrared Epsilon-Near-Zero Modes in Ultra-Thin Phononic Films," *Applied Physics Letters* 111 (2017): 091105, https://doi.org/10.1063/1.4996213.

45. M. C. Troparevsky, A. S. Sabau, A. R. Lupini, and Z. Zhang, "Transfer-Matrix Formalism for the Calculation of Optical Response in Multilayer

26999293, 2026, 10, Downloaded from https://advanced.onlinelibrary.wiley.com/doi/10.1002/adpr.70292 by University Of Delaware Library, Wiley Online Library on [23/10/2026]. See the Terms and Conditions (https://onlinelibrary.wiley.com/terms-and-conditions) on Wiley Online Library for rules of use; OA articles are governed by the applicable Creative Commons License

Systems: From Coherent to Incoherent Interference," *Optics Express* 18 (2010): 24715–24721, https://doi.org/10.1364/OE.18.024715.

46. T. Mackay and A. Lakhtakia, The Transfer-Matrix Method in Electromagnetics and Optics (Springer Cham, 2020), https://doi.org/10.1007/978-3-031-02022-3.

47. G. Kirchhoff, "I. On the Relation Between the Radiating and Absorbing Powers of Different Bodies for Light and Heat," *The London, Edinburgh, and Dublin Philosophical Magazine and Journal of Science* 20 (2009): 1–21, https://doi.org/10.1080/14786446008642901.

48. D. Wei, C. Harris, and S. Law, "Volume Plasmon Polaritons in Semiconductor Hyperbolic Metamaterials," *Optical Materials Express* 7 (2017): 2672–2681, https://doi.org/10.1364/OME.7.002672.

49. D. Wei, S. Maddox, P. Sohr, S. Bank, and S. Law, "Enlarged Growth Window for Plasmonic Silicon-Doped InAs Using a Bismuth Surfactant," *Optical Materials Express* 10 (2020): 302–311, https://doi.org/10.1364/OME.383260.

50. R. R. Senechal and J. C. Woolley, "Redetermination of the Effective Mass in Heavily-Doped n-Type InAs," *Physica Status Solidi (b)* 59 (1973): K35–K37, https://doi.org/10.1002/pssb.2220590148.

Supporting Information

Additional supporting information can be found online in the Supporting Information section.

26999293, 2026, 10, Downloaded from https://advanced.onlinelibrary.wiley.com/doi/10.1002/adpr.70292 by University Of Delaware Library, Wiley Online Library on [23/10/2026]. See the Terms and Conditions (https://onlinelibrary.wiley.com/terms-and-conditions) on Wiley Online Library for rules of use; OA articles are governed by the applicable Creative Commons License